

## A transparent waveguide chip for versatile total internal reflection fluorescence-based microscopy and nanoscopy

Anish Priyadarshi<sup>1,2,3✉</sup>, Firehun Tsige Dullo<sup>1,3</sup>, Deanna Lynn Wolfson <sup>1</sup>, Azeem Ahmad<sup>1</sup>, Nikhil Jayakumar<sup>1</sup>, Vishesh Dubey<sup>1</sup>, Jean-Claude Tinguely<sup>1</sup>, Balpreet Singh Ahluwalia <sup>1✉</sup> & Ganapathy Senthil Murugan<sup>2✉</sup>

Total internal reflection fluorescence (TIRF) microscopy is an imaging technique that, in comparison to confocal microscopy, does not require a trade-off between resolution, speed, and photodamage. Here, we introduce a waveguide platform for chip-based TIRF imaging based on a transparent substrate, which is fully compatible with sample handling and imaging procedures commonly used with a standard #1.5 glass coverslip. The platform is fabricated using standard complementary metal-oxide-semiconductor techniques which can easily be scaled up for mass production. We demonstrate its performance on synthetic and biological samples using both upright and inverted microscopes, and show how it can be extended to super-resolution applications, achieving a resolution of 116 nm using super resolution radial fluctuations. These transparent chips retain the scalable field of view of opaque chip-based TIRF and the high axial resolution of TIRF, and have the versatility to be used with many different objective lenses, microscopy methods, and handling techniques. We see this as a technology primed for widespread adoption, increasing both TIRF's accessibility to users and the range of applications that can benefit from it.

<sup>1</sup>Department of Physics and Technology, UiT The Arctic University of Norway, Tromsø, Norway. <sup>2</sup>Optoelectronics Research Centre, University of Southampton, Southampton, UK. <sup>3</sup>These authors contributed equally: Anish Priyadarshi, Firehun Tsige Dullo. ✉email: [anish.priyadarshi@uit.no](mailto:anish.priyadarshi@uit.no); [balpreet.singh.ahluwalia@uit.no](mailto:balpreet.singh.ahluwalia@uit.no); [smg@orc.soton.ac.uk](mailto:smg@orc.soton.ac.uk)

A common trade-off in microscopy is between resolution, speed, and photodamage or photobleaching. Total internal reflection fluorescence (TIRF) microscopy, however, is a rare example of a method, which improves all three simultaneously, compared to confocal microscopy. In TIRF, only the bottom  $\sim 100$  nm of the sample is excited<sup>1–5</sup>, which improves the axial resolution, eliminates out-of-focus light, and protects the bulk of the sample from photodamage. Additionally, because TIRF is a widefield technique, acquisition of a full image can occur within milliseconds. TIRF's ability to focus exclusively on a thin layer at the surface of the cell has made it an excellent tool for studying, among others, the dynamics of focal adhesions<sup>5</sup>, the inner workings of endocytosis<sup>6</sup>, the kinetics of cell surface receptors<sup>7</sup>, and docking of synaptic vesicles with neurons<sup>8</sup>.

The enabling mechanism of TIRF is the generation of a thin, exponentially decaying layer of light at a surface, called the evanescent field. When light is directed into an interface between media with a high index of refraction contrast (HIC) at a sufficiently high angle, the light is totally reflected within that interface; while the light itself does not escape from the high index material, an evanescent field is generated along the surface that the light travels<sup>2,9</sup>. The angle necessary for TIRF has traditionally been achieved using a high numerical aperture (NA) objective lens<sup>1,10,11</sup>, through a prism<sup>1,4,11,12</sup>, through the use of grating couplers<sup>13,14</sup> (<https://www.swissphotonics.net/libraries.files/09-09-17ZeptosensPWGmicroarrays.pdf>) and more recently by coupling into the side facet of optical waveguide chips<sup>15–21</sup>. These photonic chips are fabricated using technology similar to computer chips, and thus have the potential to be mass-produced at low cost. While objective lens-based TIRF is restricted to using a high NA lens, thus limiting its field of view (FOV), the evanescent field generated by waveguides is independent of the imaging pathway, enabling them to be used with any imaging objective on a standard microscope<sup>13,17,19</sup>. Furthermore, waveguide chips have been extended to super-resolution modalities, including single-molecule localization microscopy (SMLM)<sup>17,20</sup>, entropy-based super-resolution imaging (ESI)<sup>18</sup>, and structured illumination microscopy (SIM)<sup>20</sup>. The increased relative intensity due to confinement of the light within a thin waveguide is particularly well-suited for these power-hungry techniques. In addition to achieving a sub-diffraction localization precision of 75 nm, chip-based SMLM was able to do this with an unprecedented FOV of  $0.5 \times 0.5$  mm<sup>2</sup>, approximately 100 times larger than objective lens-based techniques<sup>17,18</sup>. Similarly, chip-based TIRF-SIM has surpassed the  $2\times$  resolution enhancement of conventional SIM, achieving a  $2.4\times$  resolution enhancement due to additional benefits from the fringe pattern being generated in a high index material instead of free space<sup>20</sup>.

Thus far, most chip-based microscopy has been performed on waveguides fabricated on top of opaque substrates<sup>15–17,19,20</sup>. With the sample sitting on top of the waveguide, the chips can therefore only be used with an upright microscope (Fig. 1a) because the emitted light cannot pass through the opaque substrate to the objective of an inverted microscope. On an upright microscope, however, the light must travel from the bottom of the sample where it is emitted, through the rest of the sample (which may be complex and highly scattering) and its surrounding media, and typically through a glass coverslip to the objective. This translates to aberrations in the image, not because of inferior optics but because of the scattering of light from the sample itself and from index mismatches from the medium in which cells are kept (Fig. 1a). This problem is even more pronounced for super-resolution techniques, for example in SMLM, where aberrations limit both the localization precision of the single-molecule and the resulting resolution enhancements, and in SIM where these aberrations can result in additional reconstruction artefacts.

Additionally, opaque chips have several practical handling difficulties, particularly with their use on an upright microscope<sup>11,22</sup>. Typically, a thin PDMS frame is placed on the chip around the specimen to contain the media, and a glass coverslip seals the chamber from the top enabling the use of air or water immersion media. This arrangement, however, blocks the addition of reagents or the use of micromanipulation tools during imaging, the low volume inside the chamber can be problematic for live cell imaging, and the chamber often induces tilt in the coverslip, leading to additional image aberrations. Unless the objective is designed for water, the media in the chamber induces yet more aberrations from index mismatch. Even with a water dipping objective, which solves some of these challenges, the opacity of the chip makes it impossible to check on the sample using a basic brightfield or phase-contrast microscope, so the confluency and health of cells cannot be checked prior to labelling and imaging. Thus, having a transparent chip platform (Fig. 1c) would be highly beneficial so that the sample can be more easily handled and inspected, remain open on the top for sample treatment during the experiment, and be used with a broader variety of objective lenses and microscopes.

For the design of a transparent waveguide chip compatible with these goals, the key is to match its properties as closely as possible to a standard #1.5 glass coverslip<sup>10,22</sup>. While one-dimensional slab waveguides have been previously made on coverslips<sup>3,12,21</sup>, the common borosilicate glass of these substrates is not compatible with the fabrication processes such as annealing at high temperatures. Furthermore, one-dimensional slab waveguide does not provide same possibilities like two-dimensional waveguides in terms of on-chip illumination engineering. To advance beyond basic widefield imaging, the ability to shape the propagation of light is essential. Shaping of the light through waveguide design, as with on-chip SIM<sup>20</sup>, or through the use of multiple guided modes, as shown for super-resolution radial fluctuations (SRRF)<sup>23</sup>, provides additional imaging possibilities that were not possible using the designs and fabrication methods of previous coverslip-based, one-dimensional waveguides. Super-resolution techniques, such as single-molecule localization, typically require high power ( $1–10$  KW cm<sup>-2</sup>), and the confinement of light into a 2D waveguide provides a significant advantage over the broad distribution of light in a slab waveguide. Additionally, the choice to couple light into the one-dimensional slab waveguides using a grating<sup>3,21</sup> effectively limits the waveguide to a single wavelength, making it difficult to do multicolour imaging, and restricts the propagating light to a single-mode. In the case of end-facet fibre-to-waveguide butt coupling, the input coupling losses are huge due to the high mode miss-match between the waveguide and single-mode fibre<sup>24</sup>. A wavelength-independent high coupling efficiency can be achieved using an objective lens with piezoelectric alignment stage<sup>17</sup>. Recently, this configuration was demonstrated to provide automatic input coupling to the chip which makes the set-up user-friendly<sup>25</sup>.

By choosing a substrate better suited to standard complementary metal-oxide-semiconductor (CMOS) fabrication techniques than the standard glass, and by using objective lens-based end-coupling for the light, a much broader range of imaging techniques becomes possible, although compatibility with standard sample preparation and imaging processes must of course still be maintained. Choice of a different substrate can also help ensure HIC, resulting in a larger proportion of the chip having sufficiently high intensity for imaging<sup>26</sup>. Keeping within these guidelines will result in a much more versatile and user-friendly tool thereby increasing the likelihood of adoption by the broader biological imaging community. Commercially available Zeptosens one-dimensional waveguide slides, which are based on thick transparent glass slides and are therefore

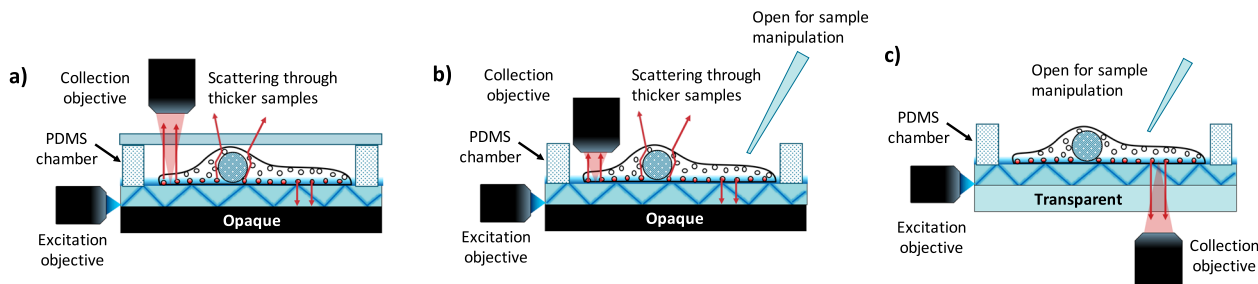


**Fig. 1 Schematic illustrating the differences between light paths in opaque versus transparent c-TIRF.** Light is coupled into the waveguide from an excitation objective lens, shown on the left side of the chip. The coupled light is reflected between the interfaces with the substrate **a** opaque with water immersion objective lens **b** opaque with water dipping objective lens and **c** transparent and the sample, keeping the light totally within the waveguide and generating an evanescent field to illuminate the bottom layer of the sample (shown as a blue line). **a, b** Using a waveguide on an opaque substrate, emitted fluorescence (red arrows) must pass through the bulk of the sample, potentially experiencing scattering or other distortions, before it can be collected by an objective located above the sample in an upright configuration. With a transparent substrate, emitted light can be collected by either an upright configuration as shown in **(a, b)** or by an inverted microscope as shown in **(c)**. With the inverted setup, the light only needs to pass through the relatively homogeneous chip rather than a distorting sample. Additionally, in **(b, c)** the area above the sample can be left open to allow for the addition of reagents or for micromanipulation during imaging. The figure is not drawn to scale for the purpose of clarity.

incompatible with high NA, short working distance objectives have already shown that there is a strong market for user-friendly TIRF technologies (<https://www.swissphotonics.net/libraries/files/09-09-17ZeptosensPWGmicroarrays.pdf>)<sup>13</sup>. Thus, further expansion into high-performance, coverslip-compatible two-dimensional waveguide TIRF technologies is likely to still be more beneficial.

In this work, we have developed a two-dimensional optical waveguide platform based on HIC waveguide materials: tantalum pentoxide on a thin, transparent fused silica substrate, which mimics standard glass coverslips and is compatible with standard CMOS mass-production processes. We show that it can be used for TIRF imaging on both upright and inverted microscopes, and demonstrate this using both fixed and living samples. Furthermore, we show that this chip platform is compatible with fluctuation-based super-resolution imaging, in particular SRRF.

## Result

**Design and characterization of transparent waveguide chip.** To ensure the highest compatibility with a wide variety of microscopes, the two-dimensional optical waveguide chips should closely match the properties of a conventional glass coverslip, including the transparency, thickness, and index of refraction (RI). Additionally, the material must be compatible with the waveguide fabrication processes, have low surface roughness, and ideally be relatively inexpensive and readily available. The borosilicate glass used for traditional coverslips is unfortunately incompatible with the higher-temperature fabrication steps (such as annealing) and has a somewhat high propagation loss<sup>27</sup>. While sapphire is both transparent and compatible with high-temperature processes, it is expensive and has an RI significantly different from that of coverslip glass ( $n_{\text{sapphire}} = 1.70$ <sup>28</sup> compared to  $n_{\text{glass}} = 1.51$  @ 633 nm<sup>29</sup>). Fused silica (as opposed to oxidized silica) is transparent at visible wavelengths, and compatible with annealing. Additionally, its RI ( $n_{\text{fusedsilica}} = 1.46$ ) is relatively close to that of glass, and its propagation losses are lower than those in glass<sup>30</sup>. Thus, fused silica was chosen as the waveguide substrate, and a thickness of 180  $\mu\text{m}$  was chosen for compatibility with #1.5 borosilicate coverslips. Spherical aberrations resulting from a difference in the optical path length through the fused silica substrate compared to a conventional coverslip, due to their different RIs, can be compensated for either through chemical mechanical polishing<sup>31</sup> to reduce the thickness of the fused silica, by adjusting the correction collar found on some higher-end microscope objectives<sup>32</sup>, or, for oil-immersion

objective lenses, by changing the RI of the immersion oil as done in this case.

c-TIRF applications benefit from a strong evanescent field with smaller penetration depth as it improves the axial resolution and produces increased fluorophore emission and enables blinking (on–off switching) for super-resolution applications. Thin waveguide geometries (e.g., 100–200 nm thickness) made from HIC materials such as  $\text{Si}_3\text{N}_4$  and  $\text{Ta}_2\text{O}_5$  produce strong evanescent fields with smaller penetration depth,<sup>17–20,26,33</sup> making them good choices for the transparent waveguide platform.  $\text{Ta}_2\text{O}_5$  has a higher RI than  $\text{Si}_3\text{N}_4$  ( $>2.1$ <sup>34</sup> compared to 2.007<sup>35</sup> at 632 nm), and as it was recently reported that  $\text{Si}_3\text{N}_4$  has a significantly higher background signal, especially for the 400–500 nm wavelength region<sup>36</sup>, we choose  $\text{Ta}_2\text{O}_5$  for the c-TIRF waveguides.

Contrary to one-dimensional slab waveguides, fabrication of two-dimensional waveguides are particularly tricky as the entire fabrication pipelines must be optimized for the fragility of the thin (180  $\mu\text{m}$ ) fused silica wafer. Handling procedures must be even more stringent because both sides of the substrate should be clean and free from scratches, as the top side hosts the optical waveguides and the emitted light will pass through the bottom side on an inverted microscope. Standard photolithography processes and ion beam etching were used to fabricate tantalum pentoxide strip waveguides on four-inch wafers, and the steps are shown in Supplementary Fig. 1a, b with additional details provided in the “Methods” section. The wafers were diced into individual chips during the back end processing, which is done in a non-cleanroom environment, and were temporarily bonded with a thick (1 mm) glass wafer (Supplementary Fig. 2) to protect them from breaking during this process. This provided mechanical stability from the pressure during wafer dicing and polishing, and could be safely removed without damaging the waveguides afterwards, without adding significant cost to the process. Finished chips on both opaque silicon and transparent fused silica substrates are shown in Fig. 2a, b. For the transparent substrate, waveguides of varying widths were examined by scanning electron microscopy (top view and cross-section shown in Fig. 2c, d) and showed no visible fabrication defects.

As the roughness of the substrate and the deposited  $\text{Ta}_2\text{O}_5$  has both a strong impact on the waveguide propagation losses and can influence the aberrations when imaging on an inverted microscope, we used an atomic force microscope (AFM) to examine the roughness both before and after deposition (Supplementary Fig. 3). While the transparent silica substrate

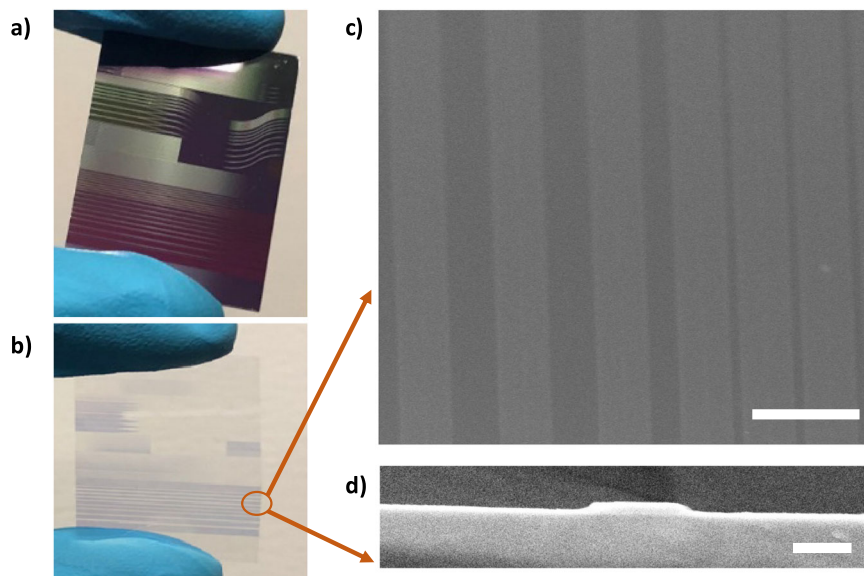


**Fig. 2 Fabricated waveguide chips on both transparent and opaque substrates.** Photographs of the fabricated waveguide chips after back-end processing on either **a** an opaque substrate or **b** a transparent substrate. SEM images showing the clean fabrication of a waveguide chip on the transparent substrate from **(c)** a top view, with a scale bar of 10  $\mu\text{m}$  and where the waveguides appear as dark lines and **(d)** a cross-section of the waveguide input facet with a scale bar of 1  $\mu\text{m}$ . The width and height of the fabricated waveguide shown in **(d)** are 1500 and 250 nm, respectively, and the sidewall angle is  $-85^\circ$ .

**Table 1 Summary of material parameters of the transparent substrate and opaque substrate with and without 250 nm thick Ta<sub>2</sub>O<sub>5</sub> film on top.**

Substrate	Roughness (rms)	Roughness after Ta <sub>2</sub> O <sub>5</sub> deposition (rms)	Refractive index by ellipsometry (at 660 nm)	Propagation loss (5 $\mu\text{m}$ wide and 250 nm strip waveguide)
Transparent fused silica (180 $\mu\text{m}$ )	0.460 nm	1.061 nm	2.164	6.4 dB $\text{cm}^{-1}$
Opaque silicon substrate (1 mm) with SiO <sub>2</sub> cladding layer (2.5 $\mu\text{m}$ )	0.178 nm	0.632 nm	2.152	3.7 dB $\text{cm}^{-1}$

Graphs and images for determining the roughness and refractive index of the substrate and film are shown in Supplementary Fig. 1.

was rougher (rms = 0.460 nm) than a standard oxidized wafer (rms = 0.178 nm), both were significantly less rough than a glass coverslip typically used for microscopy (rms = 1.5–2 nm)<sup>37</sup>. After sputtered deposition of 250 nm of Ta<sub>2</sub>O<sub>5</sub> onto the substrates, we measured the new rms surface roughness values to be 1.061 nm for the transparent substrate and 0.632 nm for the standard oxidized substrate; these measurements suggest that the roughness of the base substrate will impact the roughness after subsequent deposition steps, and ultimately will affect the final waveguide losses.

The difference between the RI of the waveguide and the surrounding medium dictates the percentage of guided-mode power that is present on the surface of the waveguide, thus it was important to measure any changes that occurred in the material during the fabrication process. The RI of the Ta<sub>2</sub>O<sub>5</sub> film deposited on the fused silica substrate was measured in the visible spectrum using a spectroscopic ellipsometer and compared with the same film deposited on an opaque substrate (Table 1 and Supplementary Fig. 4). The slightly higher RI of Ta<sub>2</sub>O<sub>5</sub> film on the transparent substrate (2.164 at 660 nm) compared to the same film on the opaque silicon substrate (2.152 at 660 nm) may be due to differences in the substrates' surface properties, including their surface roughness. While the magnitude of this index difference is not expected to affect the field strength significantly, the higher RI is actually preferable as it leads to a stronger evanescent field. The surface intensity and penetration depth of evanescent field for Ta<sub>2</sub>O<sub>5</sub> waveguide (high RI contrast) was simulated and compared

with waveguide platform made of lower RI contrast material as shown in Supplementary Fig. 5. The higher the refractive index contrast the smaller the penetration depth of the evanescent field. Moreover, HIC materials confine the light more tightly inside the waveguide and by designing thin waveguide geometry (150 nm), the surface intensity on top of the waveguide surface can be significantly enhanced (Supplementary Fig. 5).

Next, the chip's transparency was compared to a standard 170  $\mu\text{m}$  glass cover glass slips by measuring the transmission spectra of both using an optical spectrum analyzer (OSA), as shown in Supplementary Fig. 6. Relative to a glass coverslip, there is a slight reduction in transmission through the chip for visible wavelengths (400–700 nm). However, since this is caused by the higher Fresnel reflection by Ta<sub>2</sub>O<sub>5</sub> (refractive index  $\sim 2.1$ ) compared to a bare coverslip (refractive index  $\sim 1.5$ ), this is only expected to affect imaging using an external light source, and not the transmission of light from a waveguide to the microscope objective.

The final quality control check before the waveguides could be used for imaging was to measure the propagation losses using scattering analysis<sup>38</sup>. The propagation loss (Table 1) for narrow (5  $\mu\text{m}$  wide) Ta<sub>2</sub>O<sub>5</sub> waveguides on the transparent substrate was found to be 6.6 dB  $\text{cm}^{-1}$  at 660 nm, which is notably higher than for similar waveguides on opaque substrates (3.7 dB  $\text{cm}^{-1}$ ). This higher loss is mainly related to the Ta<sub>2</sub>O<sub>5</sub> film quality, which depends on the initial substrate surface quality, and in the future can be reduced by improving the substrate roughness. For wider

waveguides (>50  $\mu\text{m}$  width), the propagation losses were on the order of  $1 \text{ dB cm}^{-1}$ ; these lower losses are because the modes of the propagating light have less overlap with the roughness of the waveguide sidewalls. As a wider waveguide translates to a larger FOV, all of the c-TIRF imaging reported here used these wider, lower loss waveguides (200–500  $\mu\text{m}$ ), which are still narrow enough to ensure sufficiently high power density for imaging.

To allow for a large illuminated FOV we chose to use very wide waveguides, e.g., 200–500  $\mu\text{m}$  wide, which will simultaneously guide several modes inside. The interference of these modes creates a wavy, uneven illumination pattern, which can be evened out by translating the coupling objective lens with respect to the input facet of the waveguide over time or by scanning a galvo mirror in front of a stationary coupling objective lens (Supplementary Fig. 7a–c), but the lack of certain modes can lead to stripe-like artefacts as seen in some of the images. However, this uneven illumination pattern can be exploited for fluctuation-based super-resolution imaging, and because of the high RI of the waveguide material, the illumination patterns can contain higher spatial frequencies than with conventional free-space optics<sup>2</sup>, potentially leading to even higher resolution. The uniformity of the illumination was quantified by imaging a diluted concentration of a fluorescent dye as shown in Supplementary Fig. 7. Ignoring the edge of the waveguide, the modulation depths (variation) over the stretch of the waveguide are 15 and 12% for piezo stage and galvo mirror-based scanning systems, respectively (Supplementary Fig. 7d). This intensity modulation obtained on a transparent chip is comparable to previously published work on silicon nitride waveguide on an opaque silicon substrate, which was 16%<sup>17</sup>.

Commonly used objective lenses of the microscope are optimized for the imaging on the standard borosilicated cover glass slip platform in an inverted microscope. We performed PSF measurements of different objective lenses (20 $\times$ /0.45/air, 60 $\times$ /1.2/water immersion, and 60 $\times$ /1.49/oil immersion) for imaging using fused silica substrate. PSF of the transparent platform for different objective lenses, 20 $\times$ /0.45/air, 60 $\times$ /1.2/water immersion, and 60 $\times$ /1.49/oil immersion, are shown in Supplementary Fig. 8a–c, and corresponding full-width half maxima (FWHM) values are listed in Supplementary Table 1. PSF measurements are systematically performed on the fluorescence beads of 0.2  $\mu\text{m}$  diameter. The measured FWHMs are found to be greater than the theoretical limits of the microscope corresponding to different objective lenses. The slightly large value of FWHM could be due to the presence of aberrations in our optical system. Interestingly, the PSF measurement with 60 $\times$ /1.49/oil immersion objective lens using 1.508 refractive index immersion oil that is commonly used with borosilicate cover glass platforms resulted in broader PSF as compared to that of 60 $\times$ /1.2 water immersion lens. This is due to the difference of refractive index between the borosilicate glass (1.51) and fused silica (1.46), while the objective lenses are traditionally aberration corrected for the borosilicate glass. To address this problem, we performed simulation studies of PSF for our transparent waveguide platform, fused silica, with both 60 $\times$ /1.2/water immersion and 60 $\times$ /1.49/oil immersion objective lenses and different refractive index immersion oils (Supplementary Fig. 9). Based on the simulation studies, fused silica substrate exhibited the best PSF for the immersion oil with a refractive index of 1.62 and was found to be close to the theoretically expected value. Supplementary Fig. 10 shows the PSF measurements with 60 $\times$ /1.49/oil immersion objective lenses with our transparent waveguide platform with RI of 1.508 and 1.62 immersion oils (refractive index liquid, Cargille Labs) and the trend of the results is in agreement with the simulation results (Supplementary Fig. 9). The FWHM values for the lines profiles in Supplementary Fig. 10c are listed in Supplementary Table 2.

**Fluorescence imaging using waveguides on a transparent platform.** As our transparent platform provides imaging capability with both upright and inverted configurations, we have developed an experimental setup that integrates both these configurations (Fig. 3) thereby allowing us to directly compare images taken in both modalities. To ensure one-to-one comparison we have used identical objective lenses (60 $\times$  1.2 NA water immersion) and CMOS cameras. In addition, to reduce the impact of photobleaching between measurements in the two different modalities, low power was used for excitation and the measurements were performed consecutively. A well-like sample chamber consisting of an approximately 150  $\mu\text{m}$  thick layer of polydimethylsiloxane (PDMS) was placed on the top of the waveguide surface to hold the sample and the aqueous imaging buffer, and was sealed with a #1.5 thickness coverglass<sup>26</sup>.

While TIRF microscopy provides illumination of only the thin bottom section of the sample (100–200 nm), the emitted fluorescent light can undergo additional scatterings and refraction, causing it to appear out of focus during imaging. This phenomenon is especially pronounced in an upright configuration, as the emitted fluorescence has to travel through an inhomogeneous sample and imaging buffer before reaching the collection objective lens, thus increasing the opportunity for scattering and refraction. In contrast, when imaging in inverted mode the emitted fluorescence only needs to pass through the relatively homogeneous and non-scattering chip to reach the objective lens.

Next, to evaluate the impact of the difference in collection pathways, we have collected c-TIRF images of solutions of standard 2  $\mu\text{m}$  diameter fluorescent beads using both the upright and inverted microscopy setups. In the image of an aggregate of beads taken with the upright setup, shown in Fig. 4a, a diffuse fluorescent signal can be observed which makes it somewhat difficult to identify and to resolve the boundaries between individual beads. In comparison, a c-TIRF image of the same area acquired using the inverted configuration (Fig. 4b) shows better contrast and resolution between beads as compared to the upright configuration, since there is less scattering and refraction of the emitted light. The difference between the two modalities shows more clearly in the large aggregation of beads than it does when there are only two beads, as shown in the upper right corner within Fig. 4. This demonstrates that, for c-TIRF images of beads and other samples with high RI mismatch or scattering potential, an inverted microscopy configuration will yield images with fewer aberrations and better resolution due to the more direct path to the imaging objective. This is the main reason why most of the advanced optical microscopy used for bio-imaging application employs an inverted microscopy configuration. Thus, the enabling of an inverted configuration through the development of a transparent chip has a real impact on the image quality compared to opaque chips, which are limited to upright configurations. The transparent chip still maintains the c-TIRF advantage of the scalability of the FOV, as demonstrated in Supplementary Fig. 11, which shows c-TIRF imaging of beads over a FOV of  $635 \times 635 \mu\text{m}^2$  using a 20 $\times$  0.45 NA air objective lens.

We expanded this investigation to include biological samples and chose the relatively thick HeLa cell line (10–20  $\mu\text{m}$  thick) to emphasize the problems associated with scattering. The thin structures of actin networks in cells, here labelled with Atto647N Phalloidin, can provide a distinct, sub-diffraction-sized target to quantify the resolution of different imaging techniques in fluorescent microscopy. Fixed HeLa cells were imaged on the same dual configuration microscope as the fluorescent beads, and the averaged c-TIRF images are shown in Fig. 5. While the images from both configurations may initially appear quite similar, there

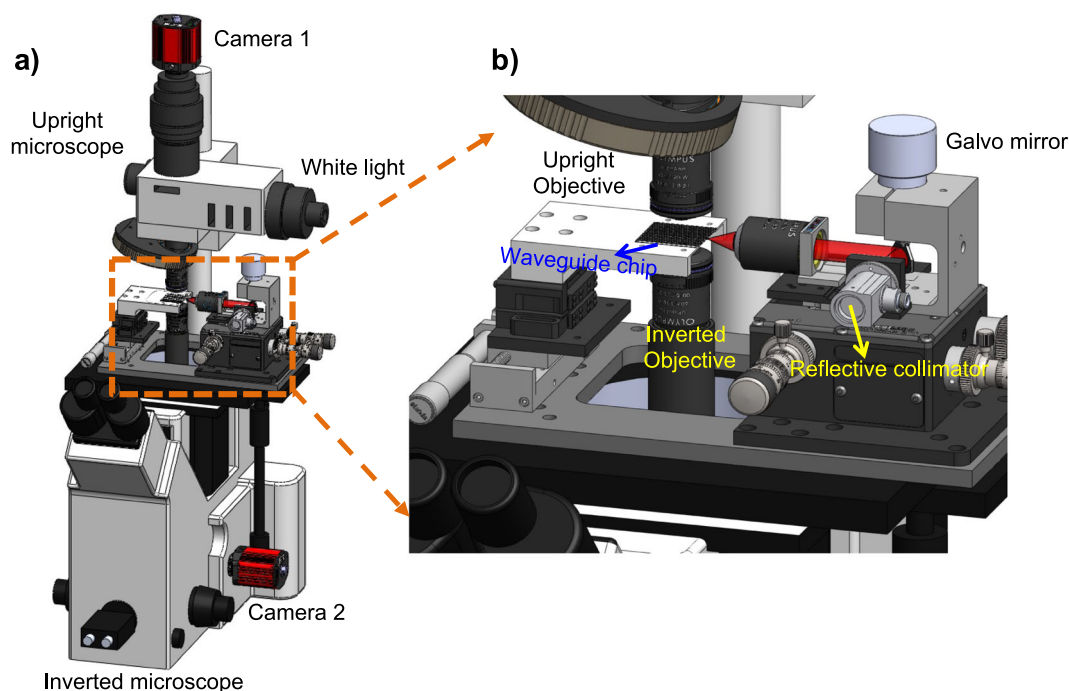


**Fig. 3 3D view of the dual-configuration microscope used for c-TIRF imaging.** **a** 3D rendering of the integrated c-TIRF microscope, where the upright microscope is above the waveguide chip and the inverted microscope is below the waveguide chip. This integrated system enables direct comparison between imaging modalities on the same sample. **b** Closeup of the waveguide chip with coupling and imaging objectives in orange dotted box. The waveguide chip holder can be rotated in X, Y, and Z to ensure it is aligned flat with respect to the imaging plane, thus avoiding uneven focus across a field of view. It also has a long travel translation stage along the Y-axis for switching from one waveguide to another waveguide on the same chip. The coupling objective, collimator, and galvo mirror are on an X-Y-Z nanometric stage separate from the main microscope to facilitate the free-space coupling of a laser into the transparent waveguide chip.

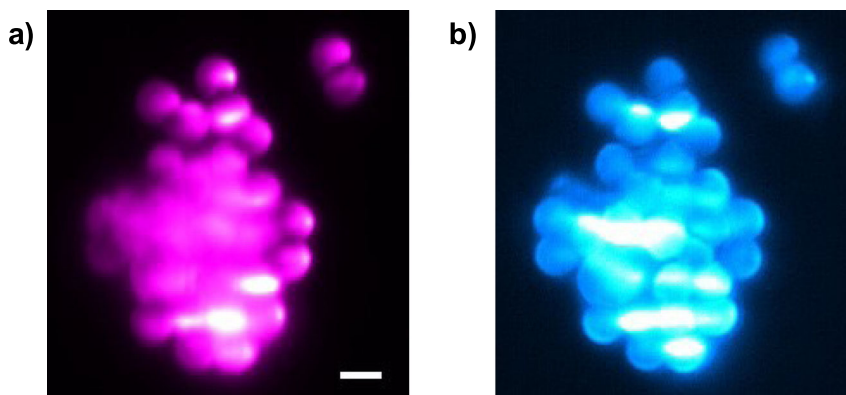


**Fig. 4 Comparison of different c-TIRF imaging setups using 2  $\mu$ m diameter fluorescent beads.** A cluster of beads was imaged using a 60 $\times$  1.2 NA water objective lens on a transparent waveguide on **a** the upright configuration and **b** the inverted configuration. The c-TIRF image with the inverted configuration in **(b)** shows a clearer separation between beads than compared to the upright configuration in **(a)**, especially in the more dense regions of the bead aggregate. This is due to the strong scattering and refraction of the emitted light as it has to pass through an inhomogeneous sample before reaching the collection objective in the upright configuration. Both images were acquired on the same waveguide in the same region and consecutively. In both cases, 1500 frames were averaged and each of these frames was acquired with 50 ms exposure time. The scale bar is 2  $\mu$ m.

appears to be a slightly higher resolution in some areas with the inverted setup (Fig. 5d) than with the upright configuration (Fig. 5c). In particular, the region under the nucleus is less visible with the upright configuration, and this relatively dark region is broader than would be expected if it was purely due to uneven waveguide modes. The blurring effect is likely due to scattering from the relatively thick and dense nucleus, which results in additional aberration and reduced collection of the emitted light. However, imaging with our inverted setup resulted in an overall slightly reduced signal compared to the upright setup, which

reduced the improvement in image quality in the thinner, less-scattering parts of the sample. We hypothesize that this is due to minor differences in the optical path length of the chip compared to the coverslip the objective was designed for, which can be compensated for by adjusting the chip thickness in future designs or by increasing the intensity or exposure time when using the current chip design to achieve a similar signal-to-noise ratio. The ability to image in both upright and inverted configurations, and the improvement under dense areas of the sample together demonstrate the utility of the transparent c-TIRF platform. The

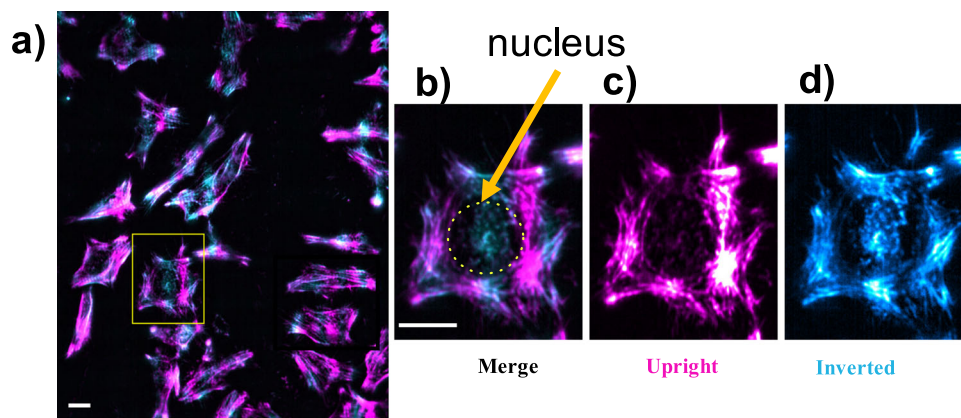


**Fig. 5 Comparison of inverted versus upright performance of c-TIRF for imaging actin in fixed HeLa cells.** Cells were imaged on a transparent waveguide using both the (c, magenta) upright and (d, cyan) inverted configurations, and the two images overlaid as shown in (a); the boxed region in (a) is enlarged in (b–d). The circled region in (b) indicates the position of the nucleus in a yellow dotted circle. With the inverted setup (d), more structure is visible under the nucleus than with the upright setup (c); this is due to the scattering and refraction of the emitted light as it passes through the bulk of an inhomogeneous sample while travelling to the upright objective, whereas the light only needs to pass through the relatively homogeneous substrate to reach the inverted objective. Both imaging modalities show relatively dark, approximately vertical regions which are due to the mode patterns in the waveguide, but the dark region under the nucleus in (c) is broader than can be explained simply by these mode patterns. For all images shown here, 60×1.2 NA water immersion objectives were used, and 1500 frames each with 50 ms acquisition times were averaged to compensate for the mode patterns. Scale bars are 10 μm.

relatively dark region in both imaging modalities due to uneven waveguide modes can be overcome by replacing the piezo stage with galvo mirror to scan the modes (Fig. 6).

Another important characteristic of the c-TIRF platform is biocompatibility. HeLa cells have previously been seen to grow on Ta<sub>2</sub>O<sub>5</sub> waveguides<sup>17</sup>, and a study of osteoblasts on various topologies of Ta<sub>2</sub>O<sub>5</sub> showed that there was no decrease in cell viability compared to glass or plastic cell culture plates, although there were some differences in cell adhesion<sup>39,40</sup>. HeLa cells could be easily grown on our transparent waveguide chips, and showed minimal cell death after 1.5 days. Interestingly, the cells show a slight preference to grow along the Ta<sub>2</sub>O<sub>5</sub> waveguides compared to the transparent silica substrate, but were observed to grow well on both surfaces (Supplementary Fig. 12). While living HeLa cells can be imaged using the transparent waveguide chips (Supplementary Fig. 13), a stage-top incubation system should be implemented in the future to maintain a physiologically relevant environment for live-cell studies.

Next, we have demonstrated the implementation of a high-NA oil immersion objective lens (60×1.49 NA) with c-TIRF image of solutions of standard 2 μm diameter fluorescent beads in the inverted configuration (Supplementary Fig. 14); due to its short working distance, it was not possible to image in the upright configuration using this objective. Based on the simulation and experimental results in Supplementary Figs. 9, 10, we used immersion oil with a RI of 1.62 (refractive index liquid, Cargille Labs). Adding the ability to use high NA lenses significantly improves the utility of the c-TIRF platform; while traditional lens-based TIRF systems are locked to this high NA, c-TIRF can be used with a low NA, large FOV lens to screen for interesting events and then be switched over to a high NA lens for enhanced resolution without ever losing the optical sectioning of TIRF.

Finally, we extended the application of the transparent waveguide platform to super-resolution optical microscopy (nanoscopy). We chose to use SRRF<sup>23</sup> as it is well-known to provide decent reconstructions at a low signal-to-noise ratio. Here, we take advantage of the fluctuations provided by varying the mode patterns in the waveguide, and instead of averaging them to acquire a standard c-TIRF image, they are processed using the SRRF algorithm in FIJI. The resulting SRRF image

(Supplementary Fig. 15b, d) shows a clear enhancement in resolution compared to the standard c-TIRF image (Supplementary Fig. 15a, c). Line profiles (Supplementary Fig. 15e, f) drawn across bundles of actin filaments in identical locations in Supplementary Fig. 15b, d highlight this even further. While the SRRF profile of the first bundle (Supplementary Fig. 15e, purple) shows two clearly resolved actin fibres, the c-TIRF profile (Supplementary Fig. 15e, green) shows only a slight separation between the same two fibres. For the second actin bundle (Supplementary Fig. 15f), c-TIRF shows only one large fibre while SRRF has the resolution to distinctly resolve two separate fibres. The overall resolution enhancement is further confirmed with Fourier ring correlation (FRC)<sup>41</sup>, which measured the resolution in the SRRF image to be 116 nm (Supplementary Fig. 16). To remove the mode patterns presented in Supplementary Fig. 15 due to uneven waveguide modes, a galvo mirror was used to scan the modes and the resulting SRRF image is shown in Fig. 6. Figure 6b, d shows a clear enhancement in resolution compared to the standard c-TIRF image (Fig. 6a, c). Line profiles (Fig. 6e) drawn across bundles of actin filaments in identical locations in Fig. 6b, d highlight this even further. To the best of our knowledge, this is the first demonstration of super-resolution waveguide-based TIRF on a transparent substrate.

## Discussion

Chip-based TIRF provides significantly improved versatility compared to traditional TIRF techniques by unlocking the restriction of the objective lens and decoupling of the excitation and emission pathways. Additionally, the inherent variation in the illumination pattern in broad waveguides makes the c-TIRF platform a natural partner for fluctuation-based super-resolution techniques, and the high RI of the waveguide enables even smaller patterns to be generated for fluctuations than is possible with free-space optics.

A major inhibitor of the utility of previous c-TIRF implementations was the opacity of the chip itself, which forced it to be used only on upright microscopes and required significantly complicated sample handling procedures. Additionally, the emitted light needed to travel along a relatively large path through the sample, subjecting it to several sources of distortion before

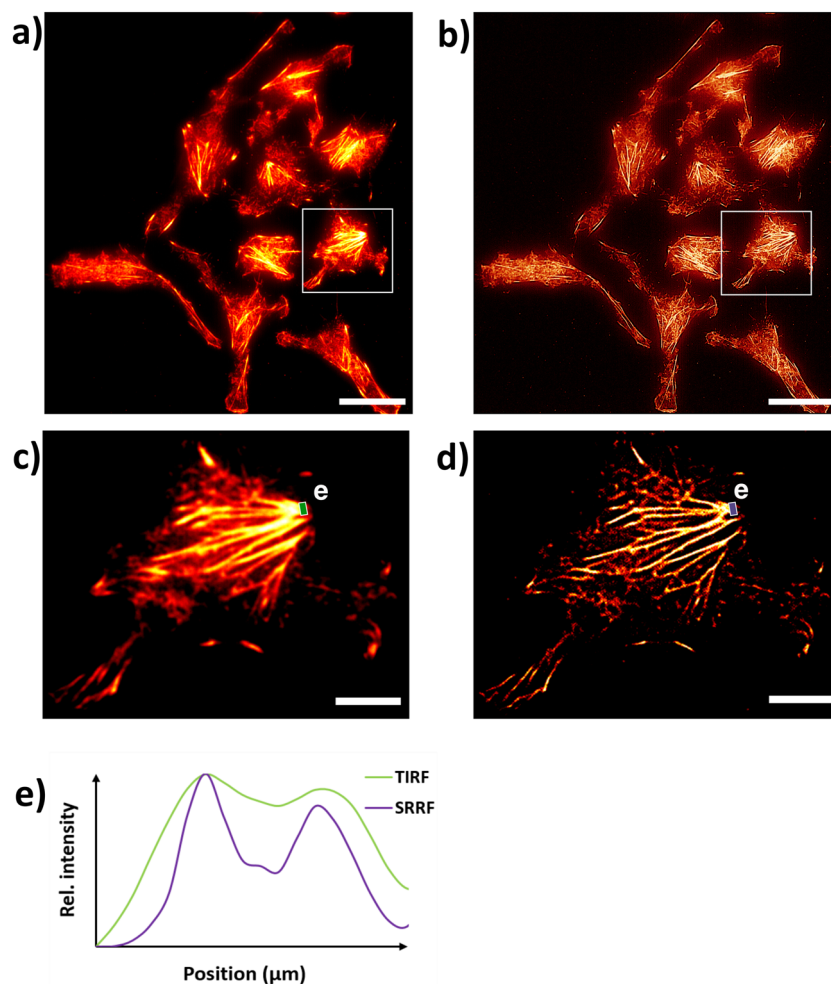


**Fig. 6 c-TIRF and super-resolved image of actin in fixed HeLa cells on a transparent waveguide.** Here, a series of images were acquired using a water immersion objective lens (60 $\times$ , 1.2 NA) on an inverted setup. **a** Shows an averaged c-TIRF image of actin in fixed HeLa cells with the corresponding super-resolved SRRF reconstruction in **(b)**. **c, d** Shows the zoomed-in region of the white boxes outlined in **(a, b)**. Intensity profiles of the green and purple lines drawn across adjacent actin filaments in **(c, d)** are plotted in **(e)** and show much clearer separation between actin fibres in the SRRF image (purple lines) compared to c-TIRF (green lines). For the SRRF image, 500 frames were used and each of these frames was acquired with a 200 ms exposure time. The scale bar in **(a, b)** is 25  $\mu\text{m}$  and in **(c, d)** is 6  $\mu\text{m}$ .

reaching the imaging objective. Here we describe a new c-TIRF platform, and its corresponding fabrication process, which completely eliminates those issues. By fabricating waveguides on a thin, transparent fused silica substrate we have matched these chips to standard glass coverslips in both their imaging and handling properties while still ensuring compatibility with a full range of CMOS mass fabrication processes and the freedom to design a variety of different waveguide shapes and sizes on a mechanically, thermally and optically superior substrate compared to standard glass coverslips. We have shown that these chips can be used on both upright and inverted microscopes on both synthetic and biological samples, and with a variety of imaging objectives, without compromising the excellent optical sectioning of traditional TIRF techniques. Chip-based TIRF can easily accommodate multiple wavelengths, so multicolour imaging and photoswitching are both easily achievable in the future<sup>17</sup>. As a proof-of-concept, we have shown 116 nm resolution using SRRF on a transparent waveguide (Supplementary Fig. 16).

A two-dimensional transparent waveguide platform based on HIC materials also increases the evanescent field intensity. To demonstrate this, we compared the single-molecule blinking and its localization precision between our fused silica transparent

waveguide platform and when borosilicate glass coverslips are employed as 1D optical waveguide<sup>3,21</sup>. These comparisons were done by depositing a dye monolayer directly on top of both the waveguide platforms. The single-molecule blinking which is the prerequisite for all SMLM was achieved using transparent waveguide platform and localization precision of 24.13 nm is attainable with the transparent platform (Supplementary Fig. 17). In contrast to the transparent waveguide platform, no blinking of the fluorophore molecules was observed with the glass coverslip platform even with four times stronger incident power (Supplementary Fig. 17). In future, it will be interesting to explore SMLM with transparent waveguide geometry, which allows using an oil-immersion objective lens. Until now all waveguide-based SMLM was performed using an upright microscopy with the highest N.A. of 1.2 using a water immersion objective lens. Both the resolution and the localization precision increase with increasing N.A. of the imaging objective lens as shown in Supplementary Fig. 18. A transparent waveguide platform can also be used for additional super-resolution techniques such as ESI, direct stochastic optical reconstruction microscopy (*d*STORM), or super-resolution optical fluctuation imaging (SOFI).

The use of CMOS-compatible fabrication for these chips means production can be scaled up for eventual mass production at a

low cost, allowing them to be used in many more labs and environments than traditional TIRF. Because of the decoupling of the emission pathway from the TIRF excitation, these chips could be combined with more durable cameras and collection optics, enabling them to be directly used in harsher environments, such as inside a humid incubator, under water, or at extremely high temperatures. Alternatively, because the fabrication is CMOS-compatible, chips could conceivably be designed to contain the waveguide, integrated filters, camera, and an LED light source as a single, integrated CMOS-based device. Additionally, as waveguide technology allows light to be sent along an innumerable variety of complex paths not possible in free-space, we see natural extensions for future designs to facilitate e.g., FRAP, photoactivation, or phototaxis along specific patterns. Our aim was to make TIRF microscopy significantly more user-friendly and accessible, and as this promising technology is increasingly adopted, we anticipate seeing even more applications in fields where TIRF was previously impractical.

## Methods

**Waveguide fabrication front end process.** Front end process flow diagram is shown in Supplementary Fig. 1a. 250 nm thick Ta<sub>2</sub>O<sub>5</sub> film was deposited using RF magnetron sputtering directly onto 4" diameter wafers of 180 μm thick transparent fused silica or of 1 mm thick silicon (with 2.5 μm SiO<sub>2</sub>). The base pressure of the deposition chamber was kept below 1 × 10<sup>-6</sup> Torr with Ar:O<sub>2</sub> flow rates of 20 standard cubic centimetre per minute (sccm): 5 sccm. A substrate temperature of 200 °C was maintained throughout the deposition time. Ta<sub>2</sub>O<sub>5</sub> films were deposited with a high deposition rate of 2.2 nm min<sup>-1</sup> as determined using a stylus profiler (KLA Tencor P-16+ model). Photolithography was used to create a photoresist mask for further dry etching to fabricate channel waveguides. First, a 1.3 μm thick layer of positive resist (Shipley S1813) was spin-coated on top of the 250 nm Ta<sub>2</sub>O<sub>5</sub> film and then prebaked at 90 °C in an oven for 30 min. Second, the prebaked photoresist was exposed under a hard chrome mask with waveguide patterns using a mask aligner (MA6, Carl Suss). The time needed to properly expose the photoresist differs depending on the substrate used (based on whether it is reflective, transmissive, or absorptive), therefore the exposure time was optimized separately for the transparent substrate (5.8 s at 20 mW cm<sup>-2</sup>) and opaque substrate (5.6 s at 20 mW cm<sup>-2</sup>). Finally, the exposed patterns were developed using MF-319 developer for 58 s.

The dry etching was performed in an ion beam system (Ionfab 300+, Oxford Instruments) using Argon gas with a flow rate of 6 sccm and Trifluoromethane (CHF<sub>3</sub>) gas with a flow rate of 12 sccm to fully etch the Ta<sub>2</sub>O<sub>5</sub> waveguides. The process beam voltage (500 V), beam current (100 mA), RF power (500 W), and substrate temperature (15 °C) were kept constant throughout the etching process. In the ion beam milling process, the substrate was placed at an angle of 45° with respect to the incident ion beam to achieve low sidewall roughness. The processed wafer was subjected to plasma-ashing with oxygen gas for 20 min to remove the photoresist. After that, the wafers were placed in a 3-zone tube furnace for annealing at 600 °C (ramp rate of 3 °C min<sup>-1</sup>–525 °C, ramp rate of 2 °C min<sup>-1</sup> from 525 to 600 °C) in an oxygen environment (2 litre min<sup>-1</sup>) for 3 h to reduce the stress and repair the oxygen deficiency created in Ta<sub>2</sub>O<sub>5</sub> during the fabrication process<sup>42</sup>.

**Waveguide fabrication back-end process.** The back-end process flow diagram is shown in Supplementary Fig. 1b. Photoresist (MICROPOSIT®S1813) was spin-coated on top of the processed wafer on both sides of the substrate to safeguard waveguides from scratching and contamination during the back-end process. Thin fused silica substrate was temporarily bonded with a thick (1 mm) glass wafer with a 4" diameter to ensure that the thin transparent wafer would not break during the back-end processing. As shown in Supplementary Fig. 2a, the thin transparent waveguide wafer was placed on the thick circular glass carrier substrate using quartz wax from Logitech (part no. 0CON-200, Melting point 66–69 °C) and heated to 80 °C for its fast melting. Constant pressure was applied after melting the wax to make sure no air bubble remained trapped and that the spreading of the wax was uniform throughout the thin transparent wafer as shown in Supplementary Fig. 2b. After that, the transparent wafer with carrier glass was diced with a diamond blade under water cooling (Isomet 5000, Buehler) into small chips.

Instead of dicing for the opaque substrate, cleaving along the crystal lattice was performed to dice the chips.

The lapping and polishing processes for the transparent and opaque chips were carried out on a Logitech LP50 system. The initial lapping step utilized a 9 μm alumina solution from 30 min to 1 h, until the waveguide end facets of the diced chips were fully visible and flat. The second lapping step utilized a 3 μm alumina solution and was performed for 30 min to reduce the surface roughness to below 3 μm. In both cases, the sample was placed against a rotating metal plate. The alumina lapping solution with 3 μm particles offered sufficient removal rates of

5 μm min<sup>-1</sup>. After lapping, the samples were polished on a different LP50 system using a diamond slurry. The surface roughness value for diced waveguide input facets was reduced from a few microns to tens of nanometres after polishing.

**AFM measurement.** The roughness of the substrates and deposited Ta<sub>2</sub>O<sub>5</sub> thin films was measured with an AFM (Cypher, Asylum Research) in amplitude modulation mode by scanning an area of 2 × 2 μm. A standard cantilever (Olympus AC160TS,  $k \approx 30 \text{ N m}^{-1}$ ,  $Q \approx 300$ ,  $f(1)0 \approx 300 \text{ kHz}$ ), was used for all experiments. A scanning rate of 1 Hz and an oscillation amplitude of ~7 nm was employed for the roughness measurements. For reconstructing the tip–sample interaction force, the amplitude and phase curves were recorded versus the tip–sample separation distance, and Sader–Jarvis–Katan formalism was used to transform the cantilever dynamics into the force versus distance curves<sup>43</sup>.

**Ellipsometry measurement.** The ellipsometric spectra of the 250 nm thick Ta<sub>2</sub>O<sub>5</sub> film on the transparent fused silica and opaque silicon substrates were collected using a J.A. Woollam VASE ellipsometer in the 400–800 nm spectral range. The measurements were performed at an angle of incidence of 55° and analyzed using the CompleteEASE ellipsometry data analysis programme. They were fitted using the Tauc–Lorentz method which is suitable for amorphous semiconductor materials<sup>44</sup>.

**Surface intensity and penetration depth of evanescent field.** The surface intensity and penetration depth of the evanescent field for Ta<sub>2</sub>O<sub>5</sub> waveguide, HIC, was simulated and compared with a waveguide platform made of low refractive index contrast material.

The surface intensity can be estimated by the percentage of guided-mode power that is present on the surface of the waveguide, top layer. Thus, we simulated the waveguide mode, as shown in Supplementary Fig. 5a, b, and quantified the percentage of guided-mode power that is present on the surface of the waveguide as presented in Supplementary Fig. 5c. A penetration depth of the evanescent field is the distance at which the intensity of the electromagnetic field drops to 1/e of its value at the interface and depends on the wavelength, effective index of the waveguide mode, and refractive index of the top layer. The penetration depth of evanescent field as a function of waveguide thickness for Ta<sub>2</sub>O<sub>5</sub> and low refractive index contrast waveguide platform is as shown in Supplementary Fig. 5d. The semi-analytical values for the penetration depth of the evanescent field of 250 nm Ta<sub>2</sub>O<sub>5</sub> the waveguide is in a range of 50–70 nm for the specific wavelengths used in this work, which are 561, 640, and 660 nm (Supplementary Table 3).

The waveguide mode was simulated with the commercial software FIMMWAVE (Photon Design, Oxford, UK), and its effective index was calculated using the full-vectorial film mode matching (FMM) method.

**Microscopy setup for c-TIRF.** Figure 3 shows the 3D schematic of the c-TIRF microscopy system developed to image in both inverted and upright directions. The microscope base is a Leica DMIRB, and the sample stage area (Fig. 3b) has been modified to work with waveguide chips. A chip is held on an aluminium holder with an open bottom, which simultaneously provides access to the upright objective above, the inverted objective below, and the coupling objective on the side. Laser excitation light (iChrome MLE, Toptica Photonics, 100 mW, 561 or 640 nm; and Cobolt Flamenco, 500 mW, 660 nm) is coupled into a single-mode fibre (P1-460Y-FC-1, Thorlabs) and collimated using a reflective collimator (RC04FC-P01, Thorlabs). The collimated light is reflected towards the coupling objective lens (Olympus 50× 0.5NA) using a galvo mirror (GVS211/M). The coupling objective lens focuses the light beam onto a side facet of the waveguide. The reflective collimator, galvo mirror, and coupling objective lens are attached on a X-Y-Z translation stage. The positioning of the laser focus on the input facet can be finely adjusted using a X-Y-Z nanometre precision stage (Nanomax 300, Thorlabs) to ensure the majority of the light is coupled into the waveguide, and can be further adjusted to change the mode patterns inside the waveguide using a piezo controller (MDT693B Open-Loop Piezo Controller, Thorlabs), for piezo-based scanning scheme. Whereas, for a galvo mirror scanning scheme, the piezo stage is kept stationary and the galvo mirror scans the mode patterns inside the waveguide with high speed compared to the piezo controller. The waveguide chip holder is attached to a single-axis, long-range linear translation stage (7T173-20-50, Standa) which is used to switch the coupling of the light between multiple waveguides on the same chip, as well as to a six-axis stage (9031-M, Newport) which can be used to eliminate tilt on the waveguide chip relative to the imaging plane, thus ensuring the entire FOV will remain in focus. Fluorescent light emitted by the sample on the waveguide is captured by either the upright or inverted objective and is filtered through a combination of longpass and bandpass filters (BLP02-561R-25, Stock#67-034; BLP01-664R-25, FF01-692/40-25, respectively, SEMROCK) to block the excitation light before being imaged onto a CMOS camera (ORCA-Flash4.0 v2, Hamamatsu). Identical objectives, cameras, and filters are used in both the upright and inverted pathways to ensure an equal comparison between imaging modalities. A summary of the imaging settings used for all of the figures is included in Supplementary Table 4.

**Propagation loss of the Ta<sub>2</sub>O<sub>5</sub> waveguides.** Propagation losses were analyzed using the scattering analysis method<sup>38</sup>. 660 nm laser light was coupled into the waveguide and propagation losses were measured by acquiring images of light scattered from the waveguide surface using a microscope setup previously described<sup>38</sup>. To avoid saturated pixels, the exposure time for the microscope's CCD camera was adjusted. The images were processed with a MATLAB programme: an average value for each image was used to find the intensity of propagating light as a function of the waveguide length, and then the result was plotted on a log scale with a linear fit to estimate the propagation loss (dB/cm).

**Sample preparation.** Two-micrometres diameter, uniformly fluorescent microspheres with an RI of 1.59, and excitation/emission wavelengths of 540 nm/600 nm (FC05F, Bang Laboratories) were used. The stock solution was diluted 1:100 in water and 500 µl of the solution was added into the PDMS well chamber on the transparent waveguide.

HeLa cells were grown in minimum essential medium (MEM) supplemented with 10% fetal bovine serum and 1% penicillin/streptomycin, in a standard humidified incubator at 37 °C with 5% CO<sub>2</sub>. Cells were seeded into the PDMS well chambers on transparent waveguides (described further in Section 3) 1–2 days before imaging. Cells used for live-cell imaging were incubated with 1 µM SiR-Actin and 10 µM verapamil (Spirochrome) in a culture medium for 1 h before washing. The culture medium was aspirated and replaced with a pre-warmed Live Cell Imaging Solution (Invitrogen) before imaging. For phalloidin labelling, HeLa cells were similarly seeded within PDMS chambers, and after 1–2 days of growth fixed for ~20 min using 4% paraformaldehyde in PBS. Cells were then washed in PBS followed by incubation with 0.1% Triton X-100 in PBS for 4 min, and washed three times in PBS for a few minutes each time. Cells were then incubated with Atto-647N phalloidin (1:33 for widefield c-TIRF, 1:100 for SRRF imaging) in PBS for 90 min.

**Image processing.** All microscopy images were processed using FIJI<sup>45,46</sup>. Image sequences with fluctuating modes were first averaged over time, followed by processing steps performed on the averaged image. Background subtraction with a rolling ball radius of 50 pixels was performed for c-TIRF images of cells. Slight differences in rotation and magnification between the cameras for the upright versus inverted camera were compensated for using the Align Image by line ROI plugin for the images of fixed cells; this allowed for direct comparison by merging/overlying channels. Images shown in this paper have been linearly adjusted for brightness and contrast. Single-channel images use a 'hot' style lookup table for improved contrast.

The super-resolved images were processed with the SRRF plugin for FIJI<sup>23</sup>. Five hundred (500) frames were used to process the SRRF images, each image having 50 ms acquisition time. A ring radius of 0.5 (default) and radially magnification of 15 were used.

**Single-molecule localization on transparent waveguide chip.** Experiments were performed using the monolayer of the Dextran Alexa fluor 647 fluorescence dye in TIRF illumination mode on both platforms (transparent waveguide chip and standard borosilicate coverslip glass). Before labelling, the surface of the waveguide and coverslip was treated with 0.01% of Poly-L-lysine (PLL) for 10 min so that fluorophores can attach to the PLL to form a uniform monolayer. A 1:100,000 concentration of the dye in PBS was sufficient to form a uniform monolayer and for a spar blinking. The fluorophores were excited by 640 nm laser and the fluorescence signal was collected by 60× (1.2NA W) objective lens. The camera exposure time was set to 30 ms.

## Data availability

The data that support the findings of this study are available from the corresponding author upon reasonable request.

Received: 14 July 2020; Accepted: 26 July 2021;

Published online: 20 August 2021

## References

- Axelrod, D. Total internal reflection fluorescence microscopy in cell biology. *Traffic* **2**, 764–774 (2001).
- Mattheyses, A. L., Simon, S. M. & Rappoport, J. Z. Imaging with total internal reflection fluorescence microscopy for the cell biologist. *J. Cell Sci.* **123**, 3621–3628 (2010).
- Hao, S. et al. TIRF microscopy with ultra-short penetration depth. *Opt. Express* **22**, 10728–10734 (2014).
- Sun, W., Marchuk, K., Wang, G. & Fang, N. Autocalibrated scanning-angle prism-type total internal reflection fluorescence microscopy for nanometer-precision axial position determination. *Anal. Chem.* **82**, 2441–2447 (2010).
- Poulter, N. S., Pitkeathly, W. T. E., Smith, P. J. & Rappoport, J. Z. In *Advanced Fluorescence Microscopy: Methods and Protocols* (ed Verveer, P. J.) 1–23 (Springer New York, 2015).
- Merrifield, C. J., Feldman, M. E., Wan, L. & Almers, W. Imaging actin and dynamin recruitment during invagination of single clathrin-coated pits. *Nat. Cell Biol.* **4**, 691–698 (2002).
- Hellen, E. H. & Axelrod, D. Kinetics of epidermal growth factor/receptor binding on cells measured by total internal reflection/fluorescence recovery after photobleaching. *J. Fluoresc.* **1**, 113–128 (1991).
- Beaumont, V. Visualizing membrane trafficking using total internal reflection fluorescence microscopy. *Biochem. Soc. Trans.* **31**, 819–823 (2003).
- Axelrod, D., Thompson, N. L. & Burghardt, T. P. Total internal reflection fluorescence microscopy. *J. Microsc.* **129**, 19–28 (1983).
- Andrea, L. S. & Daniel, A. Evanescent field excitation of fluorescence by epillumination microscopy. *Appl. Opt.* **28**, 5237–5242 (1989).
- Fish, K. N. Total internal reflection fluorescence (TIRF) microscopy. *Curr. Protoc. Cytom.* **50**, 12–18 (2009).
- Pandey, V., Gupta, S. & Elangovan, R. Compact 3D printed module for fluorescence and label-free imaging using evanescent excitation. *Methods Appl. Fluoresc.* **6**, 015007 (2017).
- Grandin, H. M., Stadler, B., Textor, M. & Voros, J. Waveguide excitation fluorescence microscopy: a new tool for sensing and imaging the biointerface. *Biosens. Bioelectron.* **21**, 1476–1482 (2006).
- Gortari, A. N. et al. Metasurface-based total internal reflection microscopy. *Biomed. Opt. Express* **11**, 1967–1976 (2020).
- Agnarsson, B., Saevær, I., Thorarinn, G. & Kristjan, L. Evanescent-wave fluorescence microscopy using symmetric planar waveguides. *Opt. Express* **17**, 5075–5082 (2009).
- Agnarsson, B., Asta, B. J., Nina, B. A. & Kristjan, L. On-chip modulation of evanescent illumination and live-cell imaging with polymer waveguides. *Opt. Express* **19**, 22929–22935 (2011).
- Diekmann, R. et al. Chip-based wide field-of-view nanoscopy. *Nat. Photonics* **11**, 322 (2017).
- Helle, yI., Coucheron, D. A., Tinguely, J.-C., ie, C. I. & Ahluwalia, B. S. Nanoscopy on-a-chip: super-resolution imaging on the millimeter scale. *Opt. Express* **27**, 6700–6710 (2019).
- Archetti, A. et al. Waveguide-PAINT offers an open platform for large field-of-view super-resolution imaging. *Nat. Commun.* **10**, 1267 (2019).
- Helle, Ø. I. et al. Structured illumination microscopy using a photonic chip. *Nat. Photonics* <https://doi.org/10.1038/s41566-020-0620-2> (2020).
- Ramachandran, S., Cohen, D. A., Quist, A. P. & Lal, R. High performance, LED powered, waveguide based total internal reflection microscopy. *Sci. Rep.* **3**, 2133 (2013).
- Reitsamer, H., Groiss, H., Franz, M. & Pflug, R. Computer-controlled impalement of cells in retinal wholemounts visualized by infrared CCD imaging on an inverted microscope. *J. Neurosci. Methods* **95**, 47–53 (2000).
- Gustafsson, N. et al. Fast live-cell conventional fluorophore nanoscopy with ImageJ through super-resolution radial fluctuations. *Nat. Commun.* **7**, 1–9 (2016).
- Thomas, D., Janusz, M., Shouyuan, S. & Dennis, P. Fiber-to-waveguide coupler based on the parabolic reflector. *Opt. Lett.* **33**, 896–898 (2008).
- Diederich, B. et al. Nanoscopy on the Chea(i)p. Preprint at *bioRxiv* <https://doi.org/10.1101/2020.09.04.283085> (2020).
- Tinguely, J.-C., Helle, yI. & Ahluwalia, B. S. Silicon nitride waveguide platform for fluorescence microscopy of living cells. *Opt. Express* **25**, 27678–27690 (2017).
- Smedskjaer, M. M. et al. Topological principles of borosilicate glass chemistry. *J. Phys. Chem. B* **115**, 12930–12946 (2011).
- Malitson, I. H. Refraction and dispersion of synthetic sapphire. *JOSA* **52**, 1377–1379 (1962).
- Doherty, R. A., Felix, J. S. & Ridge, S. C. Evaluation of a new round glass coverslip for cytological examination of cultured amniotic fluid cells. *Humangenetik* **25**, 217–220 (1974).
- Rand, M. J. & Standley, R. D. Silicon oxynitride films on fused silica for optical waveguides. *Appl. Opt.* **11**, 2482–2488 (1972).
- Suratwala, T. et al. Chemistry and formation of the beilby layer during polishing of fused silica glass. *J. Am. Ceram. Soc.* **98**, 2395–2402 (2015).
- Schwertner, M., Booth, M. J. & Wilson, T. Simple optimization procedure for objective lens correction collar setting. *J. Microsc.* **217**, 184–187 (2005).
- Albrecht, K. et al. Sensitivity enhancement of transducers for total internal reflection fluorescence. **3620**, 345–354 (1999).
- Schmitt, K., Oehse, K., Sulz, G. & Hoffmann, C. Evanescent field sensors based on tantalum pentoxide waveguides—a review. *Sensors* **8**, 711–738 (2008).
- Philipp, H. R. Optical properties of silicon nitride. *J. Electrochem. Soc.* **120**, 295 (1973).
- Coucheron, D. A., Wadduwaage, D. N., Murugan, G. S., So, P. T. C. & Ahluwalia, B. S. Chip-based resonance Raman spectroscopy using tantalum pentoxide waveguides. *IEEE Photonics Technol. Lett.* **31**, 1127–1130 (2019).

37. Chada, N. et al. Glass is a viable substrate for precision force microscopy of membrane proteins. *Sci. Rep.* **5**, 12550 (2015).
38. Lindcrantz, S. M. & Helleso, O. G. Estimation of propagation losses for narrow strip and Rib waveguides. *IEEE Photonics Technol. Lett.* **26**, 1836–1839 (2014).
39. Beline, T. et al.  $\beta$ -Ta<sub>2</sub>O<sub>5</sub> thin film for implant surface modification triggers superior anti-corrosion performance and cytocompatibility of titanium. *Appl. Surf. Sci.* <https://doi.org/10.1016/j.apsusc.2020.146326> (2020).
40. Vaidulych, M. et al. Convex vs concave surface nano-curvature of Ta<sub>2</sub>O<sub>5</sub> thin films for tailoring the osteoblast adhesion. *Surf. Coat. Technol.* <https://doi.org/10.1016/j.surfcoat.2020.125805> (2020).
41. Koho, S. et al. Fourier ring correlation simplifies image restoration in fluorescence microscopy. *Nat. Commun.* **10**, 3103 (2019).
42. Wu, C. L. et al. Low-loss and high-Q Ta<sub>2</sub>O<sub>5</sub> based micro-ring resonator with inverse taper structure. *Opt. Express* **23**, 26268–26275 (2015).
43. Chiesa, M. & Lai, C.-Y. Surface aging investigation by means of an AFM-based methodology and the evolution of conservative nanoscale interactions. *Phys. Chem. Chem. Phys.* **20**, 19664–19671 (2018).
44. Jellison, G. E. & Modine, F. A. Parameterization of the optical functions of amorphous materials in the interband region. *Appl. Phys. Lett.* **69**, 371–373 (1996).
45. Schindelin, J. et al. Fiji: an open-source platform for biological-image analysis. *Nat. Methods* **9**, 676–682 (2012).
46. Schneider, C. A., Rasband, W. S. & Eliceiri, K. W. NIH Image to ImageJ: 25 years of image analysis. *Nat. Methods* **9**, 671–675 (2012).

## Acknowledgements

The authors would like to express their appreciation to Prof. James Wilkinson (University of Southampton) for discussions on the waveguide platform. We thank Sebastian Alberti (UiT) for help with the AFM experiments and Neil Sessions (University of Southampton) for fabrication equipment and SEM imaging. The authors would like to thank Øystein Ivar Helle and David Andre Coucheron for their valuable suggestions. The authors would like to thank Luis Enrique Villegas Hernandez (UiT) for helping in the schematic drawings. This research was funded by the European Research Council Proof of Concept project (H2020, ERC PoC 789817), Research Council of Norway BIOTEK 2021 (Nano-Path, Project No. 285571), and “The Future Photonics Hub” (UK EPSRC grant EP/N00762X/1).

## Author contributions

B.S.A., G.S.M. and A.P. conceived this project. G.S.M. and B.S.A. supervised and provided funding for the project. A.P. characterized the materials properties and fabricated the waveguide chip. B.S.A., F.T.D., J.C.T., and A.P. contributed to the chip design. J.C.T.

assisted with the SEM and AFM analysis. F.T.D. and N.J. characterized the waveguide losses. F.T.D., A.A., and N.J. built the imaging setup and performed the experiments. F.T.D., D.L.W. and N.J. analyzed the imaging data. D.L.W. and V.D. prepared biological samples. The paper was mainly written by A.P., F.T.D. B.S.A. and D.L.W. with comments from all co-authors.

## Competing interests

B.S.A. has applied for two patents for chip-based optical nanoscopy, “Super-Resolution Imaging (dSTORM on chip)” IPO, UK, application number 1606268.9, (2016) and “SIM-on-chip”, UK patent application number 1705660.7, (2017). B.S.A. is a co-founder of the company Chip NanoImaging AS, which commercializes on-chip super-resolution microscopy systems. All other authors declare no competing interests.

## Additional information

**Supplementary information** The online version contains supplementary material available at <https://doi.org/10.1038/s43246-021-00192-5>.

**Correspondence** and requests for materials should be addressed to A.P., B.S.A. or G.S.M.

**Peer review information** *Communications Materials* thanks the anonymous reviewers for their contribution to the peer review of this work. Primary Handling Editors: Aldo Isidori. Peer reviewer reports are available.

**Reprints and permission information** is available at <http://www.nature.com/reprints>

**Publisher's note** Springer Nature remains neutral with regard to jurisdictional claims in published maps and institutional affiliations.



**Open Access** This article is licensed under a Creative Commons Attribution 4.0 International License, which permits use, sharing, adaptation, distribution and reproduction in any medium or format, as long as you give appropriate credit to the original author(s) and the source, provide a link to the Creative Commons license, and indicate if changes were made. The images or other third party material in this article are included in the article's Creative Commons license, unless indicated otherwise in a credit line to the material. If material is not included in the article's Creative Commons license and your intended use is not permitted by statutory regulation or exceeds the permitted use, you will need to obtain permission directly from the copyright holder. To view a copy of this license, visit <http://creativecommons.org/licenses/by/4.0/>.

© The Author(s) 2021